

Integrated *LCC* Compensation Topology for Wireless Charger in Electric and Plug-in Electric Vehicles

Weihan Li, *Student Member, IEEE*, Han Zhao, Siqi Li, *Member, IEEE*, Junjun Deng, *Member, IEEE*, Tianze Kan, and Chunting Chris Mi, *Fellow, IEEE*

Abstract—This paper presents an integrated *LCC* compensation topology for electric vehicle/plug-in hybrid electric vehicle wireless chargers. The effect of the coupling between the additional coil and the main coil on the *LCC* compensation topology is studied. The proposed topology will reduce the size of the additional coil and make the system more compact with extremely high efficiency. The basic characteristics of the proposed topology are analyzed based on fundamental harmonic approximation. Furthermore, based on the steady-state model, three categories of operation modes are presented and analyzed. In order to realize zero-voltage switching, the series capacitor C_2 on the secondary side is tuned. A numerical method is used to analyze the impact of different values of ΔC_2 on the turnoff current, and the best value of C_2 is chosen to build a prototype to verify the analysis.

Index Terms—Current source, electric vehicle (EV), operation modes, wireless power transfer (WPT), zero-voltage switching (ZVS).

Manuscript received July 31, 2014; revised September 27, 2014; accepted November 11, 2014. Date of publication December 18, 2014; date of current version May 15, 2015. This work was supported in part by a U.S. Department of Energy Graduate Automotive Technology Education Grant, in part by the U.S.–China Clean Energy Research Center-Clean Vehicle Consortium, DENSO International, in part by the University of Michigan, and in part by the China Scholarship Council.

This paper has supplementary downloadable material available at <http://ieeexplore.ieee.org> provided by the authors. The material is a Word file containing: 1. appendix; 2. simulated waveforms of MOSFET at switching transition; 3. specifications of the capacitors; 4. experiment kit; and 5. experimental waveforms of four operation modes. The size of the file is 6.0 MB. Contact chrismi@umich.edu for further questions about this work.

W. Li was with the Mechanical and Automotive Engineering Department, Hefei University of Technology, Hefei 230009, China. He is now with the Department of Electrical and Computer Engineering, University of Michigan, Dearborn, MI 48128 USA (e-mail: weihanli1988@gmail.com).

H. Zhao is with the Mechanical and Automotive Engineering Department, Hefei University of Technology, Hefei 230009, China.

S. Li is with the Electrical Engineering Department, Kunming University of Science and Technology, Kunming 650500, China (e-mail: lisiqi00@gmail.com).

J. Deng is with the Department of Electrical and Computer Engineering, University of Michigan, Dearborn, MI 48128 USA, and also with the School of Automation, Northwestern Polytechnical University, Xi'an 710072, China (e-mail: dengjunjun1985@gmail.com).

T. Kan and C. C. Mi are with the Department of Electrical and Computer Engineering, University of Michigan, Dearborn, MI 48128 USA (e-mail: chrismi@umich.edu; tkan@umich.edu).

Color versions of one or more of the figures in this paper are available online at <http://ieeexplore.ieee.org>.

Digital Object Identifier 10.1109/TIE.2014.2384003

I. INTRODUCTION

THE technology of wireless charging, also referred to as wireless power transfer (WPT) or inductive power transfer (IPT), has been successfully applied at the low power level, such as applications for biomedical implant devices [1]–[4] and smartphones [5]. Along with the fast growing interest in electric vehicles (EVs) and plug-in hybrid electric vehicles (PHEVs), wireless charging, as a new way of charging batteries, has drawn the attention of researchers, car manufacturers, and customers recently [6], [7]. Compared to conductive power transfer (usually plug-in), WPT is more convenient, weather proof, and electric shock protected. Some companies, such as WiTricity, Evatran, Qualcomm, etc., have developed products which can transfer power at 3.3 kW with an acceptable efficiency. However, there is still more research work that needs to be done to further optimize efficiency, reduce cost, increase misalignment tolerance, and reduce the size of the WPT chargers.

WPT was first discovered by Nikola Tesla [8]. The basic principle of WPT is that the power transfers through electromagnetic field which is generated by the high frequency current in the transmitter coil. The receiver resonant circuit should have the same resonant frequency as that of the transmitter resonant circuit. A better explanation of this principle had been given by the Massachusetts Institute of Technology and verified by using self-resonant coils in a strongly coupled magnetic resonance regime [9]. There are many research areas in WPT, such as compensation network and circuit analyses [10]–[16], coil design techniques for large gap and misalignment tolerance [17]–[20], link optimization for high efficiency [15], [21], [22], control methods [23], [24], and foreign object detection and safety issues [23], [25]. Among them, compensation topology is very important because it helps to adjust resonant frequency, minimize the VA rating of power supply, improve coupling and power transfer capability, and achieve high efficiency [26]. As for the EV/PHEV application, the coupling coefficient varies with the changing of the vehicle ground clearance and misalignments. This will result in the variations of the circuit parameters and resonant frequencies for some compensation topologies. Therefore, it is of significant importance to design an appropriate compensation topology for EV/PHEV wireless chargers.

Based on the way the capacitors connected to the transmitting and receiving coils, four basic compensation topologies labeled as SS, SP, PS, and PP are widely adopted, where the first S or P represents the capacitor in series or parallel with the transmitter

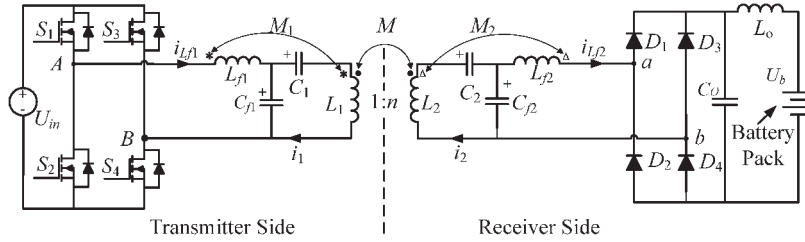


Fig. 1. Integrated *LCC* compensation topology.

coil and the second S or P stands for capacitor in series or parallel with the receiver coil. A systematic analysis of these topologies can be found in [14] and [27]–[29]. The selection of the compensation topology is dependent on the application. In [28], an optimized method was proposed to select the compensation topology from an economic perspective. The results showed that the SS and SP topologies were more suitable for high power transmission and the SS compensation topology requires less copper. However, the way to realize soft switching to reduce the switching loss is not considered in this paper. In [14], it indicated that the SS compensation topology seemed to be the best topology because the system can work at a frequency independent of the coupling coefficient and load. However, the PP compensation topology was adopted in their work because a parallel compensated transmitter could provide a large current and a parallel compensated receiver had the current source characteristic which was more suitable for battery charging. This is correct when the system is operated at the designed resonant frequency. However, the resonant condition will change with the change of the coupling coefficient and load condition. It is widely accepted that WPT system can get maximum efficiency when it works at the resonant frequency. For the SS topology, there may be one or two resonant frequencies depending on the coupling coefficient [30]. This is similar to bifurcation phenomena [14], which is inevitable for the four basic compensation topologies and brings difficulties to controller design.

Some other novel compensation topologies have been put forward in the literature. A series–parallel–series compensation topology was proposed in [29]. This particular topology, which was composed of one capacitor in series and another in parallel with the transmitter coil and of one capacitor in series with the receiver coil, had the characteristics of both SS and PS topologies. As a parallel capacitor is involved, the resonant condition will vary with the change of the load condition, and the zero phase angle of the power supply will not be realized when the load deviates from the designed value. In [31], an *LCL* parallel resonant circuit was applied for WPT. In [32], the *LCL* network was used in both transmitter and receiver sides. It makes the track (transmitter) have a constant current characteristic. This is essential for a WPT system with multiple pickups (receivers). Another compensation topology called *CLCL* network was proposed in [33]. In [34], the *CLCL* was applied in both transmitter and receiver sides, and a mathematical model was proposed. Due to the symmetrical topology and phase-modulated control method, the IPT system could achieve bidirectional power transfer. However, the inductances of the additional inductors are equal to or larger than the inductances of the main coils in these topologies. Furthermore, additional space is needed to place these inductors.

An integrated *LCC* compensation topology is proposed in this paper. The compensation topology as shown in Fig. 1 consists of one inductor and two capacitors, and together with the main coil, it formed a structure similar to an *LCL*-T network at both the transmitter (primary) and receiver (secondary) sides. The inductor (called additional inductor or additional coil in this paper) is coupled with the main coil (transmitter coil or receiver coil) on the same side. Therefore, the additional coil and the main coil can be integrated together, and additional space for additional inductors is not needed. This integrated structure can also transfer the same amount of power with smaller additional inductances, compared with one that is not integrated. With this proposed topology, the resonant frequency is still independent of both the coupling coefficient and load condition. Both the output current and the current on the transmitter coil are constant, irrelevant to load condition. When the WPT system works near the resonant frequency, it can realize power transfer on different operating conditions by controlling the input voltage.

Based on fundamental harmonic approximation (FHA), the analysis of the integrated *LCC* compensation topology is presented, and the basic characteristics are described in Section II. The open-circuit case is analyzed in Section III. The operation modes based on steady-state analysis are discussed in Section IV. A numerical method of tuning the circuit to realize zero-voltage switching (ZVS) is introduced in Section V. Experimental and simulation results are compared in Section VI. The conclusion is in Section VII.

II. AC ANALYSIS

The proposed integrated *LCC* compensation topology is shown in Fig. 1. The transmitter side consists of a high frequency inverter and a compensation resonant circuit, which is composed of an *LCC* compensation network and the transmitter coil. The inverter has a full bridge which is formed by four power MOSFETs ($S_1 \sim S_4$). L_{f1} , C_{f1} , and C_1 constitute the *LCC* compensation network. The receiver side has a symmetrical *LCC* compensation resonant circuit, rectifier, and LC filter network. In this topology, not only the two main coils, L_1 and L_2 , are coupled to each other, but also the main coil and the additional coil on the same side are coupled with each other (namely, L_1 is coupled with L_{f1} , and L_2 is coupled with L_{f2}). The mutual inductances are M , M_1 , and M_2 , respectively,

$$M = k\sqrt{L_1 L_2}, \quad M_1 = k_1\sqrt{L_1 L_{f1}}, \quad M_2 = k_2\sqrt{L_2 L_{f2}} \quad (1)$$

where k , k_1 , and k_2 are the coupling coefficients.

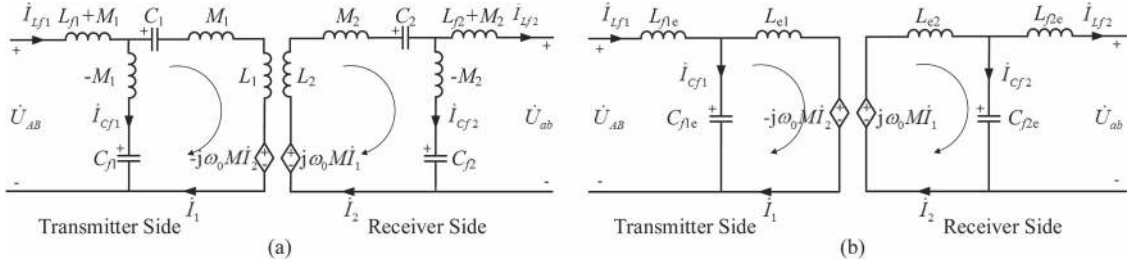


Fig. 2. Equivalent circuit. (a) Equivalent decoupled circuit model of the integrated LCC compensation topology. (b) Simplified equivalent circuit model of the integrated LCC compensation topology.

M_1 and M_2 are considered as constant, while M varies with the changing of the vehicle ground clearance and misalignment. In this paper, the range of the coupling coefficient is limited between 0.14 and 0.30 according to the coil design. Generally, the WPT system for PHEV/EV has a large leakage inductance but a small mutual inductance. Only the mutual inductance has contribution to the power transfer. Therefore, it is essential to compensate the self-inductance. Usually, the self-inductance is compensated by adding a series capacitor. For simplicity, in this paper, the main coils on both the transmitter and receiver sides are designed as the same.

In order to get the basic characteristics of the LCC compensation topology, in the alternating current analysis, the square-wave input voltage and output voltage are replaced by their first fundamental sinusoidal equivalents. The power transferred is assumed to be only through the fundamental component, and the contribution of all the high-order harmonics is ignored. All of the components used in this section are ideal, and only the continuous operation mode is considered. The two main coils L_1 and L_2 can be regarded as a transformer which can be equivalent to two decoupled circuits containing controlled sources. Therefore, the decoupled model of the compact wireless charger system can be obtained, as shown in Fig. 2(a). Assume that the circuit in Fig. 2 is driven by a sinusoidal voltage source, of which the angular frequency is ω . The circuit can be simplified by the following equations:

$$L_{f1e} = L_{f1} + M_1 \quad (2)$$

$$L_{f2e} = L_{f2} + M_2 \quad (3)$$

$$L_{e1} = L_1 + M_1 - 1/(\omega^2 C_1) \quad (4)$$

$$L_{e2} = L_2 + M_2 - 1/(\omega^2 C_2) \quad (5)$$

$$C_{f1e} = C_{f1}/(\omega^2 M_1 \cdot C_{f1} + 1) \quad (6)$$

$$C_{f2e} = C_{f2}/(\omega^2 M_2 \cdot C_{f2} + 1). \quad (7)$$

We can find that both the transmitter and receiver sides are a simple LCL resonant converter. One of the characteristics of LCL resonant converters is that the output current is constant, only related to the input voltage, if it works at the resonant frequency. The detailed analysis about the LCL resonant converter was discussed in [35] and [36]. As for this work, on the transmitter side, we assume that

$$L_{f1e} = L_{e1} \quad (8)$$

$$\omega_0 = 1/\sqrt{L_{f1e}C_{f1e}}. \quad (9)$$

From (2) and (9), the following relationship can be obtained:

$$\omega_0 = 1/\sqrt{L_{f1e}C_{f1e}} = 1/\sqrt{L_{f1}C_{f1}}. \quad (10)$$

From (2), (8), and (10), the following equation can be derived:

$$L_1 - L_{f1} = 1/(\omega_0^2 C_1). \quad (11)$$

From (10) and (11), once L_1 , L_{f1} , C_{f1} , and C_1 are determined, the resonant frequency will be fixed if we neglect the variations of inductances caused by the change of the relative position between the transmitter and receiver sides and the variations of the capacitances caused by temperature variation. Therefore, the resonant frequency is independent of the coupling coefficient and load condition.

By Kirchhoff's laws, it is easy to obtain

$$\dot{I}_1 = \frac{\dot{U}_{AB}}{j\omega_0 L_{f1e}} \quad (12)$$

$$\dot{I}_{Lf1} = \frac{M\dot{I}_2}{L_{f1e}}. \quad (13)$$

Similarly, on the receiver side, when $L_{f2e} = L_{e2}$ and $\omega_0 = 1/\sqrt{L_{f2e}C_{f2e}}$, the following equations can be obtained:

$$\dot{I}_{Lf2} = \frac{M\dot{I}_1}{L_{f2e}} \quad (14)$$

$$\dot{I}_2 = -\frac{\dot{U}_{ab}}{j\omega_0 L_{f2e}}. \quad (15)$$

Substituting (1) and (15) and (1) and (12) into (13) and (14), respectively, we can obtain

$$\dot{I}_{Lf1} = -\frac{k\sqrt{L_1 L_2} \dot{U}_{ab}}{j\omega_0 L_{f1e} L_{f2e}} \quad (16)$$

$$\dot{I}_{Lf2} = \frac{k\sqrt{L_1 L_2} \dot{U}_{AB}}{j\omega_0 L_{f1e} L_{f2e}}. \quad (17)$$

Take \dot{U}_{AB} as reference, and define

$$\dot{\delta} = \frac{\dot{U}_{AB}}{U_{AB}} \quad (18)$$

where U_{AB} is the rms value of the input voltage. It is obvious that $\dot{\delta}$ has features of the unit vector.

As \dot{U}_{ab} is a passive voltage, its direction is determined by the conduction mode of the diodes $D_1 \sim D_4$ of the rectifier. It should be in phase with \dot{I}_{Lf2} so that the following equation can be obtained:

$$\dot{U}_{ab} = U_{ab} \frac{\dot{\delta}}{j}. \quad (19)$$

Then, (12) and (15)–(17) can be expressed as

$$\dot{I}_1 = \frac{U_{AB}}{j\omega_0 L_{f1e}} \dot{\delta} = \frac{U_{AB}}{j\omega_0 (L_{f1} + M_1)} \dot{\delta} \quad (20)$$

$$\dot{I}_2 = \frac{U_{ab}}{\omega_0 L_{f2e}} \dot{\delta} = \frac{U_{ab}}{\omega_0 (L_{f2} + M_2)} \dot{\delta} \quad (21)$$

$$\dot{I}_{Lf1} = \frac{k\sqrt{L_1 L_2} U_{ab}}{\omega_0 L_{f1e} L_{f2e}} \dot{\delta} = \frac{k\sqrt{L_1 L_2} U_{ab}}{\omega_0 (L_{f1} + M_1)(L_{f2} + M_2)} \dot{\delta} \quad (22)$$

$$\dot{I}_{Lf2} = \frac{k\sqrt{L_1 L_2} U_{AB}}{j\omega_0 L_{f1e} L_{f2e}} \dot{\delta} = \frac{k\sqrt{L_1 L_2} U_{AB}}{j\omega_0 (L_{f1} + M_1)(L_{f2} + M_2)} \dot{\delta}. \quad (23)$$

Current I_1 on the transmitter coil L_1 is constant and only related to input voltage U_{AB} . This is very important if the transmitter coil transfers power to several receiver coils at the same time. Furthermore, when a PHEV/EV with a wireless charger is parked, the coupling coefficient of the main coils will be determined. As a result, the output current I_{Lf2} is also constant, which only depends on the input voltage. This is suitable for battery charging.

From (18) and (22), it is obvious that the phase difference between input current \dot{I}_{Lf1} and input voltage \dot{U}_{AB} is zero. The power factor is 1. Therefore, the delivered power can be expressed as

$$P = \frac{\sqrt{L_1 L_2}}{\omega_0 (L_{f1} + M_1)(L_{f2} + M_2)} \cdot k U_{AB} U_{ab} \quad (24)$$

where U_{AB} and U_{ab} are the rms values of the input voltage and output voltage. The receiver side main coil size is limited by the space of the bottom of the car. Therefore, the sizes of the main coils and their inductances, L_1 and L_2 , are limited. This will result in a limitation for the output power of the WPT system. It can be seen from (24) that designing proper inductances of the additional coils and proper couplings between the additional coils and the main coils is important to obtain the desired power. Moreover, if delivering the same power from the transmitter side to the receiver side, the inductances of the additional coils will be smaller, compared with the one that has no couplings between the additional coils and the main coils.

III. OPEN-CIRCUIT ANALYSIS

As indicated by (23), the output current is related to input voltage U_{AB} , coupling coefficient k of the two main coils, and component parameters if the system operates at resonant frequency ω_0 . The system is a current source, independent of the load. Fig. 3 shows the open circuit of the system. The equivalent circuit of the sending side is the same as that shown in Fig. 2. However, as an open circuit, the current on L_{f2} is zero, and the receiving side equivalent circuit is different. The inductance L_{f2} does not join the resonant circuit, but this does not change the resonant frequency of the resonant circuit according to the previous analysis. It just affects the voltage before the rectifier because of the coupling between L_2 and L_{f2} .

If the input voltage is a cosine waveform as shown in the following:

$$u_{AB} = \sqrt{2} U_{AB} \cos(\omega_0 t) \quad (25)$$

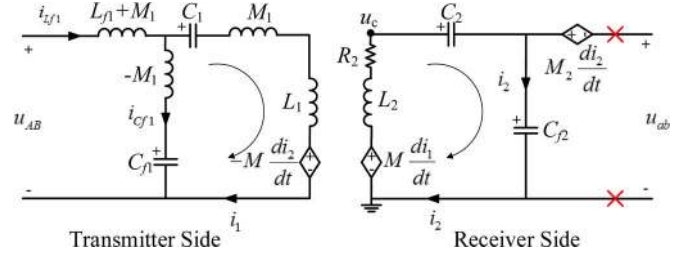


Fig. 3. Open-circuit condition of the wireless charger.

then for the receiver side, the following equation can be derived:

$$\frac{d^2 u_C}{dt^2} + \omega_0^2 u_C = \frac{\omega_0^2 M}{L_{f1} + M_1} \sqrt{2} U_{AB} \cos(\omega_0 t) \quad (26)$$

$$u_C = A \sin(\omega_0 t + \varphi) + \frac{\omega_0 M}{\sqrt{2}(L_{f1} + M_1)} U_{AB} t \sin(\omega_0 t) \quad (27)$$

where u_C is the total voltage on the receiver side capacitors C_2 and C_{f2} . A and φ in (27) are determined by the initial condition.

According to (27), the voltage on the capacitors will increase with time. This is not allowed. In practice, there will be always internal resistances in the circuit. For simplicity, the internal resistances of the circuit are equivalent to the resistances of the main coils (L_1 and L_2), and the differential equation will be

$$\frac{d^2 u_C}{dt^2} + \frac{R_2}{L_2} \frac{du_C}{dt} + \omega_0^2 u_C = \frac{\omega_0^2 M}{L_{f1} + M_1} \sqrt{2} U_{AB} \cos(\omega_0 t) \quad (28)$$

where R_2 is the equivalent resistance of the receiver side in series with the main coil and is usually very small, $R_2 < 4L_2/C$, if $2\gamma = R_2/L_2$. Considering the initial condition, the voltage on the capacitors is

$$u_C(t) = -e^{-\gamma t} \frac{ML_2\omega_0^2}{\sqrt{\omega_0^2 - \gamma^2} R_2 (L_{f1} + M_1)} \sqrt{2} U_{AB} \sin \times \sqrt{(\omega_0^2 - \gamma^2)t} + \frac{ML_2\omega_0}{R_2 (L_{f1} + M_1)} \sqrt{2} U_{AB} \sin(\omega_0 t). \quad (29)$$

The voltage on the capacitors will be steady over time as the second component of (29) showed. However, the voltage will be high enough to cause the capacitors to break down if the battery is disconnected with the wireless charger suddenly when it is in operation. Therefore, open-circuit protection is necessary for the integrated LCC compensation topology. In practice, a voltage sensor can be used to detect the voltage on the secondary parallel capacitor C_{f2} . This voltage will be compared with a threshold to control a two-way switch which is connected with nodes a and b . With this method, the open circuit protection is realized in the laboratory but not discussed in further detail in this paper due to page limits.

On the other hand, due to the resistance of the system, the power will only transfer to the battery when the input voltage is

high enough. For the open circuit, when the system is in steady state, the voltage before the rectifier is

$$u_{ab} = u_{Cf2} - u_{Lf2} = \frac{C_2}{C_2 + C_{f2}} \frac{L_2 + M_2}{L_{f1} + M_1} \frac{M\omega_0}{R_2} \sqrt{2} U_{AB} \sin(\omega_0 t). \quad (30)$$

The battery voltage is U_b . If $|u_{ab}| < U_b$, there will be no power output. Therefore, U_{AB} should be bigger than a certain value as described in (31) to ensure power transfer

$$U_{AB} > \frac{U_b}{\sqrt{2}} \frac{C_2 + C_{f2}}{C_2} \frac{L_{f1} + M_1}{L_2 + M_2} \frac{R_2}{M\omega_0}. \quad (31)$$

IV. OPERATION-MODE ANALYSIS

The operation of the integrated LCC compensation network for WPT is complex due to the high-order system and the resonant mechanism that the system has the same resonant frequency with and without inductor L_{f2} . The resonant circuit without L_{f2} is formed when the diodes of the rectifier on the receiver side are all off. The system can operate in several stages within one switching cycle, depending on the circuit component parameters, the coupling coefficient between the two main coils, the input voltage, and the load conditions (output voltage), when the operation frequency is fixed at the resonant frequency. Owing to the symmetry, only a half switching cycle should be analyzed. In Fig. 1, the diodes of the rectifier on the receiver side only conduct when the voltage between nodes a and b is higher than the battery voltage. Characterized by the voltage between nodes a and b , there are three possible resonant stages, namely, positive clamped stage (stage P), negative clamped stage (stage N), and open stage (stage O), in the half cycle when S_1 and S_4 are on and S_2 and S_3 are off. As the proposed compensation topology is controlled by the input voltage, the WPT system will pass through four operation modes successively when the input voltage increases from zero to the maximum value. The operation modes are categorized by the conduction statuses of the rectifier as cutoff mode (CUTOFF), discontinuous conduction mode (DCM), and continuous conduction mode (CCM). Depending on the different sequential combinations of the three stages, DCM can be divided into DCM1 and DCM2.

The example of the circuit parameters used in this section is listed in Tables I and II in Section V.

A. Resonant Stages

The six equivalent circuit models of the integrated LCC compensation topology over a full cycle are given in Fig. 4. According to the analysis in Section III, it is necessary to consider the resistances of the circuit. In the following sections, the resistances of the circuit are equivalent to the resistances connected to the main coils as R_1 and R_2 shown in Fig. 4, and only the first half cycle is analyzed.

1) Open Stage (Stage O): Stage O, as shown in Fig. 4(b), occurs when all of the diodes of the rectifier are off and the current on L_{f2} is zero. Inductor L_{f2} does not join the

TABLE I
SPECIFICATIONS OF THE WIRELESS CHARGER

Spec / Parameter	Design Value
Input DC voltage	≤ 450 V
Output battery voltage	300V~500V
Coils material	800 strands AWG 38 Litz wire
Main coils dimension	600x600mm
Additional coils dimension	220x220mm
Nominal gap	150 mm
X-misalignment tolerance ¹	300 mm
Y-misalignment tolerance ¹	125 mm
Switching frequency	95 kHz
Maximum power	6 kW
Full power at maximum misalignment	2.6 kW
Maximum efficiency	96.5%

¹X- or Y- misalignment tolerance is defined when the misalignment in the other direction is set to zero.

TABLE II
CIRCUIT PARAMETERS OF THE WIRELESS CHARGER¹

Parameter	Design Value	Measured Value
Transmitter coil inductance L_1 ¹	260 μ H	250~255 μ H
Receiver coil inductance L_2 ¹	260 μ H	254~260 μ H
Coupling coefficient of L_1 and L_2 : k	0.14~0.30	0.13~0.30
Transmitter side additional inductor L_{f1} ¹	36.4 μ H	39~40 μ H
Receiver side additional inductor L_{f2} ¹	36.4 μ H	39~40 μ H
Mutual inductance between L_1 and L_{f1} : M_1 ¹	23 μ H	26.5~27 μ H
Mutual inductance between L_2 and L_{f2} : M_2 ¹	23 μ H	22.5~23 μ H
Transmitter side series capacitor C_1	12.6nF	13.0nF
Receiver side additional capacitor ΔC_2	1nF	1nF
Receiver side series capacitor $C_2' = C_2 + \Delta C_2$	13.6nF	14.0nF
Transmitter side parallel capacitor C_{f1}	77.1nF	76.2nF
Receiver side parallel capacitor C_{f2}	77.1nF	76.2nF

¹The inductances of the main coils and additional coils and the mutual inductances between main coil and additional coil will slightly change when the position of the transmitter and receiver changes due to the impact of the ferrites.

resonance with other circuit components, and neither does the battery, but as mentioned before, the system still has the same resonant frequency as other stages. During Stage O, the voltage between nodes a and b is lower than the battery voltage U_b . The differential equations can be expressed in matrix form as

$$\dot{x} = A_1 x + B_1 u \quad (32)$$

where

$$A_1 = \frac{1}{\chi^I} \begin{pmatrix} 0 & a_{12}^I & a_{13}^I & a_{14}^I & a_{15}^I & a_{16}^I & a_{17}^I & 0 \\ 0 & 0 & \chi^I a_{23}^I & 0 & 0 & 0 & 0 & 0 \\ 0 & a_{32}^I & a_{33}^I & a_{34}^I & a_{35}^I & a_{36}^I & a_{37}^I & 0 \\ 0 & a_{42}^I & a_{43}^I & a_{44}^I & a_{45}^I & a_{46}^I & a_{47}^I & 0 \\ 0 & 0 & 0 & \chi^I a_{54}^I & 0 & 0 & 0 & 0 \\ \chi^I a_{61}^I & 0 & \chi^I a_{63}^I & 0 & 0 & 0 & 0 & 0 \\ 0 & 0 & 0 & \chi^I a_{74}^I & 0 & 0 & 0 & 0 \\ 0 & 0 & 0 & 0 & 0 & 0 & 0 & 0 \end{pmatrix} \quad (33)$$

$$x = [i_{L_{f1}} \ u_{C_1} \ i_1 \ i_2 \ u_{C_2} \ u_{C_{f1}} \ u_{C_{f2}} \ i_{L_{f2}}]^T \quad (34)$$

$$u = [U_{AB} \ U_{ab}]^T \quad (35)$$

¹The specification of the capacitor are listed in supplementary materials available at <http://ieeexplore.ieee.org>.

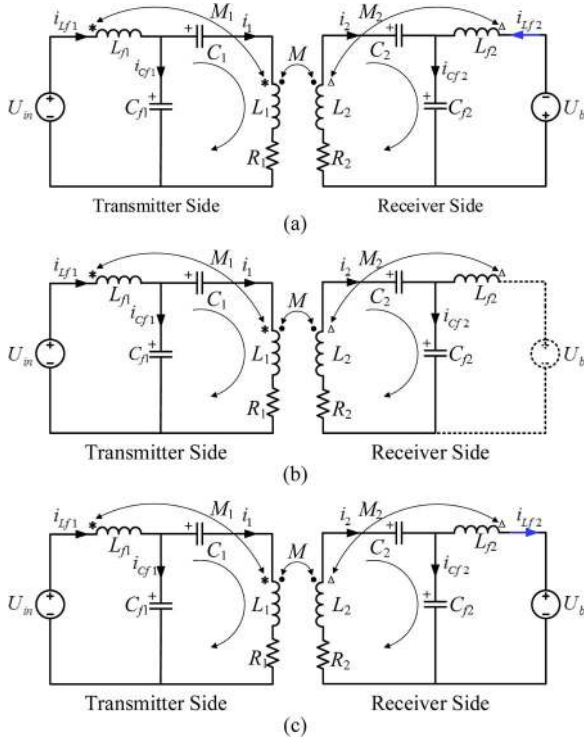


Fig. 4. Equivalent circuit models of the integrated LCC compensation topology over one half cycle*. The first half cycle: (a) Stage N, (b) Stage O, and (c) Stage P. The second half cycle is omitted. * U_{in} is the square-wave input voltage, and U_b is the battery voltage.

$$B_1 = \frac{1}{\chi^T} \begin{bmatrix} b_{11}^I & 0 & b_{13}^I & b_{14}^I & 0 & 0 & 0 & 0 \\ 0 & 0 & 0 & 0 & 0 & 0 & 0 & 0 \end{bmatrix}^T. \quad (36)$$

The elements in the matrices and other parameters are shown in the appendix.²

2) Negative Clamped Stage (Stage N): When the voltage between nodes a and b is negative and higher than the battery voltage, diodes D_1 and D_4 are off, while D_2 and D_3 are on as shown in Fig. 1, and the battery will be connected to the circuit in reverse, as shown in Fig. 4(a). Similarly, referring to the appendix, the following equation can be obtained:

$$\dot{x} = A_2x + B_2u. \quad (37)$$

3) Positive Clamped Stage (Stage P): When the voltage between nodes a and b is positive and higher than the battery voltage, diodes D_1 and D_4 will be turned on while D_2 and D_3 will be turned off. As shown in Fig. 4(c), the battery is directly connected to the resonant circuit. According to the appendix, the equation is

$$\dot{x} = A_2x + B_3u. \quad (38)$$

B. Operation Modes

When operating near the resonant frequency and with the same load condition, the integrated LCC compensation wireless charger system passes through four operating modes as shown in Fig. 5 with the input voltage increasing. The first

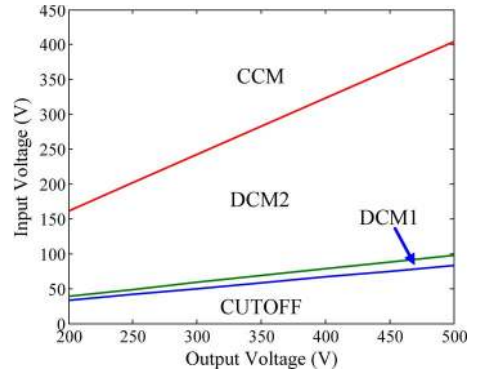


Fig. 5. Operation mode distribution when $k = 0.3$.

one is the cutoff mode (CUTOFF), followed by discontinuous conduction mode I (DCM1), discontinuous conduction mode II (DCM2), and continuous conduction mode (CCM). They are divided into the following three categories: CUTOFF, DCM, and CCM. The equations describing the modes are boundary value problems of ordinary differential equations. It is not possible to give analytical solutions for such high-order differential equations. Therefore, in this work, the results are based on numerical solutions.

1) Cutoff Mode (CUTOFF): There is no power transfer to the battery during the cutoff mode, and only stage O is involved in this mode. The input voltage is small enough comparing to the output voltage, and therefore, the voltage between nodes a and b never reaches U_b . This is caused by the resistances in the circuit and imperfect compensation. The equivalent circuit can be represented by Fig. 4(b), and the waveforms are shown in Fig. 6(a). The equation describing the steady state of the cutoff mode is (32) with boundary condition $x(0) = -x(T/2)$. This constraint boundary condition fits all of the operation modes.

2) DCM: There are two cases of the DCM as shown in Fig. 6(b) and (c). For case one (DCM1), which is after the cutoff mode, the system passes through stage O, stage N, and stage O successively (O–N–O) in the first half cycle as shown in Fig. 6(b). The equations describing it are

$$\begin{cases} \dot{x} = A_1x + B_1u, & 0 \leq t \leq t_1 \\ \dot{x} = A_2x + B_2u, & t_1 \leq t \leq t_2 \\ \dot{x} = A_1x + B_1u, & t_2 \leq t \leq T/2. \end{cases} \quad (39)$$

With the increase of input voltage, the WPT system operation mode changes from DCM1 (O–N–O) to DCM2 (N–O–P). In this process, the system will pass through a unique mode, namely, N–O. This mode is the boundary of DCM1 and DCM2, and it can be categorized into either of the two DCMs.

DCM2 mode, as shown in Fig. 6(c), occurs when the input voltage rises to a level beyond DCM1 mode, and the equations are

$$\begin{cases} \dot{x} = A_2x + B_2u, & 0 \leq t \leq t_1 \\ \dot{x} = A_1x + B_1u, & t_1 \leq t \leq t_2 \\ \dot{x} = A_2x + B_3u, & t_2 \leq t \leq T/2. \end{cases} \quad (40)$$

3) CCM: When the input voltage is high enough, the diodes of the rectifier will conduct all the time. The statuses of the circuit will shift between the negative clamped stage (N) and positive clamped stage (P). The system will pass through N

²The appendix is provided in supplementary material available at <http://ieeexplore.ieee.org>.

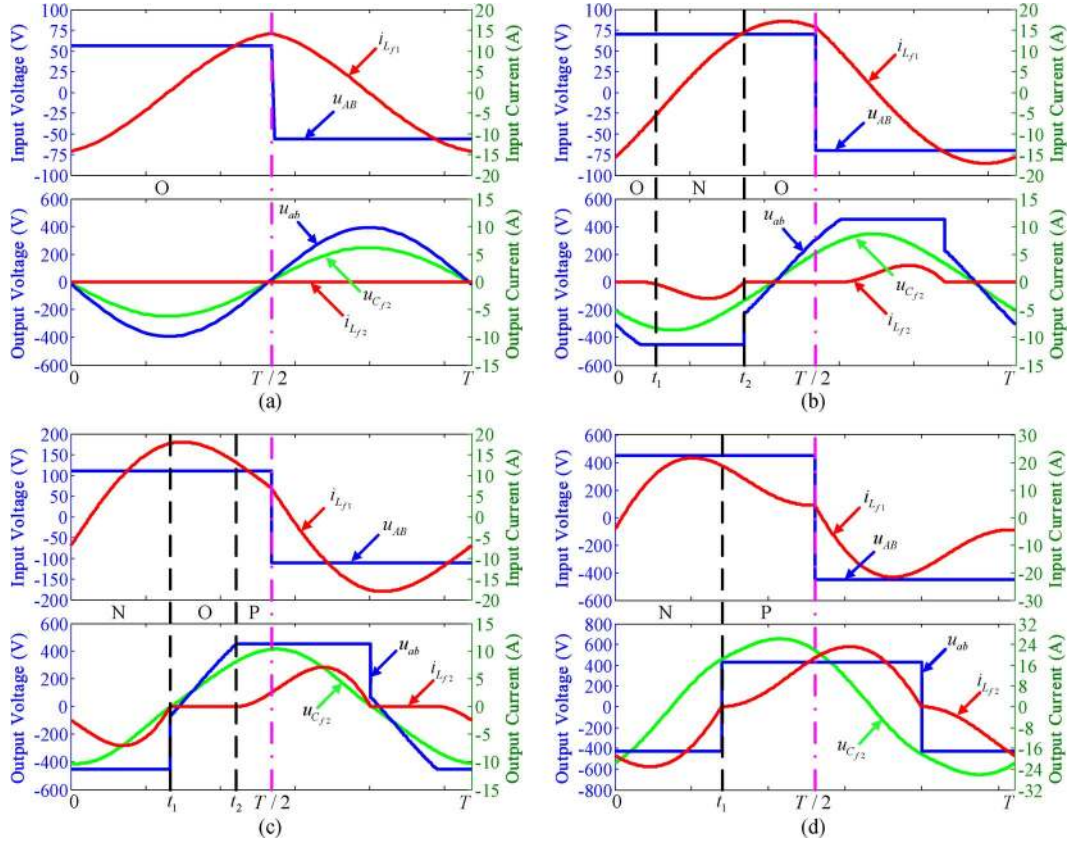


Fig. 6. Theoretical waveforms of different modes: (a) CUTOFF, (b) DCM1, (c) DCM2, and (d) CCM.

and P (N-P) in sequence during the first half resonant cycle as shown in Fig. 6(d). The equations are shown as follows:

$$\begin{cases} \dot{x} = A_2x + B_2u, & 0 \leq t \leq t_1 \\ \dot{x} = A_2x + B_3u, & t_1 \leq t \leq T/2. \end{cases} \quad (41)$$

The equations above can be solved using the numerical method, and the values of any states at any time can be obtained. Based on the aforementioned analysis, it is easy to get the output power and efficiency as

$$P_{\text{out}} = \frac{2}{T} \int_0^{T/2} (u_{ab}(t) \cdot i_{L_{f2}}(t)) dt \quad (42)$$

$$\eta = \frac{P_{\text{out}}}{P_{\text{in}}} = \frac{\int_0^{T/2} (u_{ab}(t) \cdot i_{L_{f2}}(t)) dt}{\int_0^{T/2} (u_{AB}(t) \cdot i_{L_{f1}}(t)) dt}. \quad (43)$$

It can be seen that both the output power and efficiency of the WPT system are related to the operation mode. Fig. 7 illustrates the relationship between efficiency and operation mode. With the increasing input voltage, the efficiency will increase sharply during DCM1 mode, and the rate of increase slows down when the system enters into DCM2 mode. At the end of the DCM2 mode and the entire CCM mode, the efficiency will be stabilized at the maximal efficiency.

The fundamental element approximation is accurate enough when the system is operating at CCM. However, if the system is operating at DCM modes, the error cannot be ignored. Therefore, it is essential to determine the range of different operation

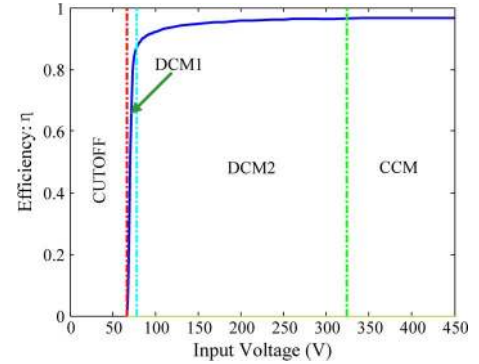


Fig. 7. Relationship between efficiency and operation modes when $k = 0.3$.

modes with various output voltage (battery voltage). The misalignments are inevitable in the wireless charger for EV/HEV; thus, it is of significant importance to analyze the impact of various coupling coefficients on the range of each operation mode.

Assuming that the input voltage is between 0 and 450 V and the output voltage is between 300 V and 500 V, the coupling coefficient varies from 0.14 to 0.30 depending on the vehicle ground clearance and misalignments. The operation mode distribution with different coupling coefficients is illustrated in Fig. 8. The lines in the figure are the boundaries of different operation modes with varying coupling coefficients. The legend, $k = 0.30$ CUTOFF/DCM1, means this line is the boundary of cutoff mode and DCM1 mode when the coupling coefficient is 0.30. The other legends have similar meanings. As can be seen in Fig. 8, the boundary input voltages increase linearly

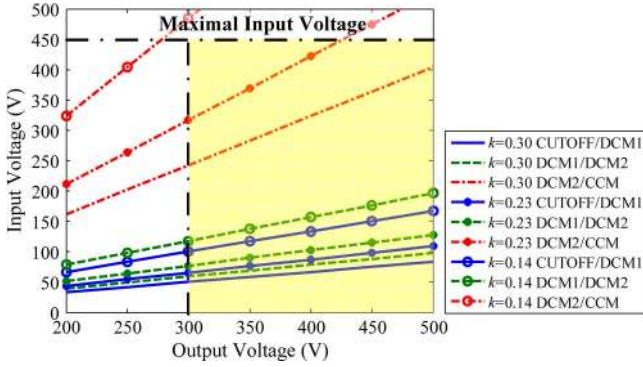


Fig. 8. Operation mode distribution with different coupling coefficients.

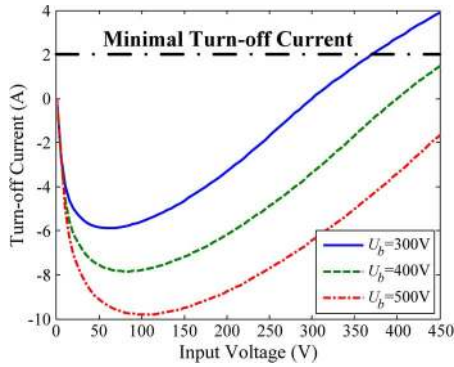


Fig. 9. Turnoff current when $\Delta C_2 = 0$.

with the output voltage rising. It also illustrates that the input voltage boundaries increase with the decrease of the coupling coefficients. Moreover, the system almost works in the DCM modes and cutoff mode over the whole input voltage range when the coupling coefficient is very small, like $k = 0.14$.

V. NUMERICAL METHOD TO TUNE CAPACITOR C_2 FOR ZVS

In this paper, MOSFETs are chosen as the switching components of the full bridge converter. The turnoff switching loss is very small since the parasitic parallel output capacitance of the MOSFET is able to hold the voltage close to zero during the turnoff transition. However, there are two major switching losses during the MOSFET turn-on transition: One is the loss induced by the diode reverse recovery process, and the other is the loss of the energy stored in the MOSFET output capacitance. Both of them can be mitigated if the MOSFETs are turned on at ZVS condition [37]. To realize ZVS, the body diode should conduct before the MOSFET does. This means that the MOSFET should be turned on at a negative current. According to the aforementioned analysis, at the end of the first half cycle, S_1 and S_4 will be turned off while S_2 and S_3 will be turned on, and at the end of the cycle, the opposite happens. Therefore, at the end of the first half cycle, the current on L_{f1} should be positive. This current is called turnoff current in this paper.³

³The simulated waveforms of the turn-on and turnoff transitions of one MOSFET are provided in the supplementary material available at <http://ieeexplore.ieee.org>.

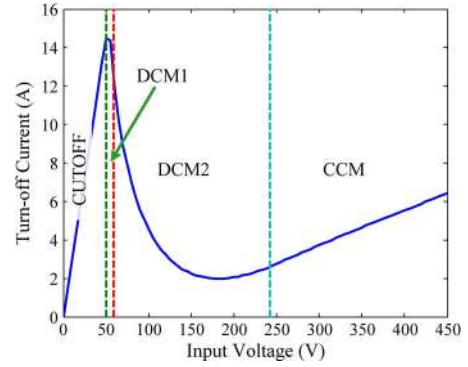


Fig. 10. Relationship of turnoff current and operation modes when $\Delta C_2/C_2 = 0.08$, $k = 0.30$, and $U_b = 300$ V.

In order to ensure MOSFET ZVS turn-on in the main operation modes (DCMs and CCM), the turnoff current should be large enough to discharge the junction capacitors within the dead time, which can be expressed as [38]

$$I_{\text{OFF}} > \frac{2C_{\text{oss}}U_{AB,\text{max}}}{t_{\text{dead}}}. \quad (44)$$

Here, $U_{AB,\text{max}}$ is the maximum input voltage, C_{oss} is the MOSFET junction capacitance, and t_{dead} is the dead time.

In this paper, Fairchild FCH041N60E N-channel MOSFET was chosen as the transmitting side inverter switches. Based on the parameters of this kind of MOSFET, the turnoff current should be larger than 2 A.

If the parameters of the proposed wireless charger are designed exactly according to the rules described before, most of the time, the turnoff current will be below the minimal turnoff current as shown in Fig. 9, and the system will operate at ZCS condition. The switching losses during MOSFET turn-on transition cannot be ignored, so it is essential to find an effective way to guarantee that the MOSFETs turned on at ZVS condition. As mentioned before, the system benefits from the fixed resonant frequency, and it is controlled by controlling the input voltage. Thus, it is not recommended to tune the switching frequency to realize MOSFET ZVS turn-on when the system is running. Another way is to change the parameters of the circuit slightly to make the input impedance of the resonant circuit inductive. Increasing the secondary series capacitor C_2 is a simple way to realize ZVS.

Before tuning capacitor C_2 , the other parameters of the integrated LCC compensation wireless charger system should be designed. At the beginning, the parameters of the system are designed roughly based on the analysis in the previous sections and then modified using a finite-element method when considering the couplings of the main coils and additional coils. The wireless charger specifications are given in Table I. As some of the work is related to the coil design, which is not the main purpose of this paper, the designed values of the wireless battery charger are listed in Table II.

The relationship between the turnoff current and operation modes is shown in Fig. 10. The turnoff current increases linearly with the input voltage rising during the cutoff mode and then changes in the form of a high-order polynomial after entering the DCM modes. In the end, the turnoff current is approximately linear with the input voltage during the CCM mode.

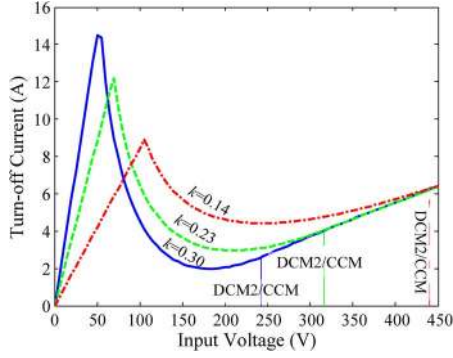


Fig. 11. Effect of coupling coefficient on turnoff current at $\Delta C_2/C_2 = 0.08$ and $U_b = 300$ V. * The vertical lines are the boundaries of DCM2 and CCM for different coupling coefficients.

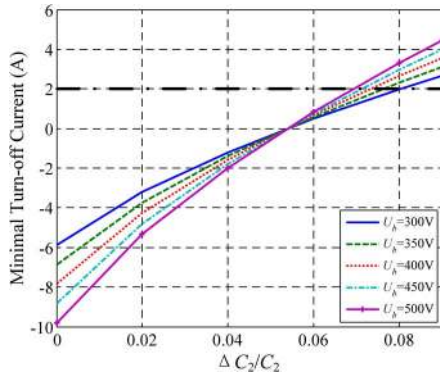


Fig. 12. Relationship between minimal turnoff current and $\Delta C_2/C_2$ with different battery voltages.

The turnoff currents in DCMs and CCM are what we should be concerned about. It can be seen that the minimum turnoff current occurs when the system operates in the DCM2 mode. The fundamental element approximation is not appropriate in this situation.

The minimum turnoff current increases with the decrease of the coupling coefficient at the condition of the same ΔC_2 and same battery voltage as shown in Fig. 11. If the system works in the CCM mode at all of the coupling coefficients (when the input voltage is higher than 440 V in Fig. 11), the turnoff current curves at different coupling coefficients will overlap with each other. Based on the aforementioned results, only the minimal turnoff current of the maximal coupling coefficient should be considered to determine the second series capacitor increment ΔC_2 .

The relationship of the turnoff current and battery voltage is complicated. It can be seen from Fig. 9 that the higher battery voltage has a smaller minimal turnoff current, but with the increase of ΔC_2 , the minimal turnoff current of a higher battery voltage will increase faster than the lower one. Finally, the former is larger than the latter. This is indicated in Fig. 12. For the same battery voltage, the minimal turnoff current will increase with the increase of ΔC_2 . From the simulation results, it can be concluded that the turnoff current will be larger than 2 A during the whole operation range when $\Delta C_2/C_2 = 0.08$. According to Table II, $C_2 = C_1 = 12.6$ nF, and $\Delta C_2 \approx 1$ nF. Then, the tuned secondary series capacitor $C'_2 \approx 13.6$ nF.

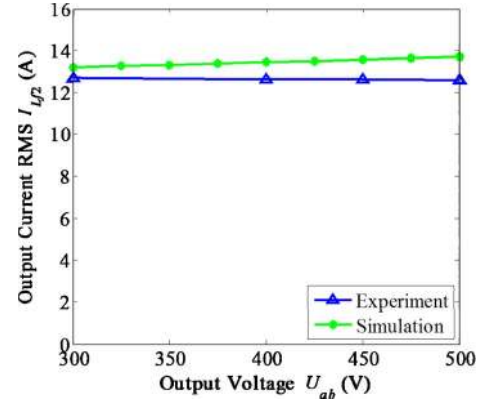


Fig. 13. Experimental and simulated output currents (rms values) vary with the change of the output voltage when the coils are aligned and the input voltage is 450 V.

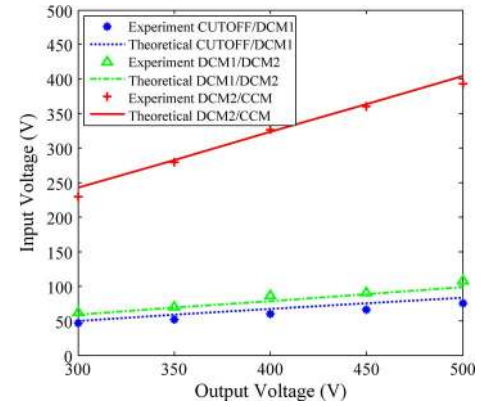


Fig. 14. Comparison of the mode boundaries from experiment and simulation when $k = 0.3$ ($X = 0$ mm).

VI. EXPERIMENTAL RESULTS

According to the parameters in Tables I and II and the aforementioned analysis, a 6-kW prototype is built.⁴ The measured parameters are slightly different from the design values due to the component tolerances. The self-inductances and mutual inductances are given in ranges because, when the relative position of the transmitter and receiver changes, they will slightly change due to the impact of the ferrites which are used to enhance the coupling. Due to the difference between the measured parameters and designed parameters, it is hard to choose the operating frequency. In this paper, the operating frequency is chosen near the designed resonant frequency, and at this frequency, the system can achieve the highest efficiency when the transmitter and receiver are aligned. Both the transmitter and receiver contain two coils, one main coil (L_1 or L_2) and one additional coil (L_{f1} or L_{f2}), which are integrated together. This is related to the coil design [19], [20] which is not discussed in this paper.

Fig. 13 shows the experimental and the simulated output current I_{Lf2} (rms value) as a function of load change when the coils are perfectly aligned and input voltage $U_{AB} = 450$ V.

⁴The experiment kit, coil structure, and experimental waveforms of different modes are provided in supplementary material available at <http://ieeexplore.ieee.org>.

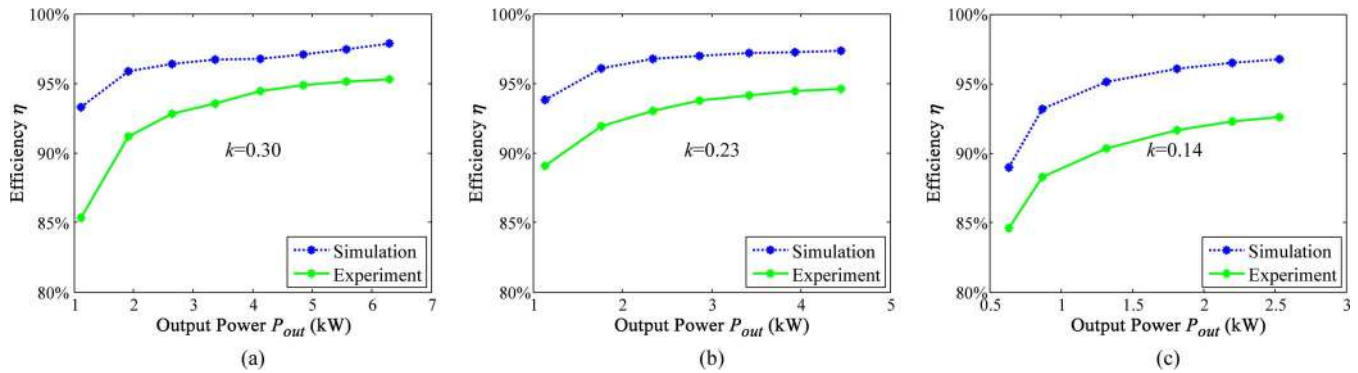


Fig. 15. Simulated and experimental efficiencies at different X-misalignment. (a) $X = 0$ mm, (b) $X = 200$ mm, and (c) $X = 325$ mm.

When the output voltage changes from 300 to 500 V, the experimental and simulated output currents are almost constant. However, a slight variation is inevitable due to the nonlinearity of the system parameters, parasitic parameters, high-order harmonics, and different power losses at different conditions.

The comparison of the mode boundaries of experimental results and simulation results is given in Fig. 14. It can be seen that they are matched well.

Fig. 15 shows the comparison of the simulated and the experimental efficiency at different X-misalignments. The measured efficiency is from the dc power source to the battery. The maximal measured efficiency is 95.3%, and the maximal simulated efficiency is 97.8%. The losses in the ferrites and aluminum shields are not considered in the simulation, so relatively, the simulated efficiency is 2%–3% higher than the experimental efficiency. It is reasonable to believe that the ferrite and aluminum shield losses are around 2%–3%.

VII. CONCLUSION

A new integrated LCC compensation topology for the PHEV/EV wireless charger has been proposed in this paper. The additional inductors are integrated with the main coils. This structure will spare the space which is needed for additional inductors and can transfer the same amount of power with smaller additional inductances compared with the one which is not integrated. Based on FHA, the topology still has a characteristic of constant current output, independent of the load. Moreover, the resonant frequency is also independent of coupling coefficient k and load conditions. The operation modes of the proposed topology are analyzed based on steady-state analysis. The WPT system will go through the four modes CUTOFF, DCM1, DCM2, and CCM successively with the rise of the input voltage. A numerical method was introduced to tune the receiver side series capacitor C_2 to realize ZVS condition for the MOSFET. A 6-kW prototype was built to verify the analysis results. The measured efficiency was as high as 95.3% from the dc power source to the battery.

In practice, it is almost impossible to integrate the additional inductors and main coils without inducing cross-couplings, although they are quite small. The impact of the couplings between L_{f1} and L_2 , L_{f2} and L_1 , and L_{f1} and L_{f2} will be our future work. Additional future work will include the realization of open-circuit protection and parameter optimizations.

REFERENCES

- [1] A. K. RamRakhyani, S. Mirabbasi, and C. Mu, "Design and optimization of resonance-based efficient wireless power delivery systems for biomedical implants," *IEEE Trans. Biomed. Circuits Syst.*, vol. 5, no. 1, pp. 48–63, Feb. 2011.
- [2] R. R. Harrison, "Designing efficient inductive power links for implantable devices," in *Proc. Int. Symp. Circuits Syst.*, 2007, pp. 2080–2083.
- [3] S. Ping, A. P. Hu, S. Malpas, and D. Budgett, "A frequency control method for regulating wireless power to implantable devices," *IEEE Trans. Biomed. Circuits Syst.*, vol. 2, no. 1, pp. 22–29, Mar. 2008.
- [4] K. Van Schuylenbergh and R. Piers, *Inductive Powering: Basic Theory and Application to Biomedical Systems*. New York, NY, USA: Springer-Verlag, 2009.
- [5] E. Waffenschmidt, "Wireless power for mobile devices," in *Proc. 33rd IEEE INTELEC*, 2011, pp. 1–9.
- [6] M. Yilmaz and P. T. Krein, "Review of battery charger topologies, charging power levels, infrastructure for plug-in electric and hybrid vehicles," *IEEE Trans. Power Electron.*, vol. 28, no. 5, pp. 2151–2169, May 2013.
- [7] H. H. Wu, A. Gilchrist, K. Sealy, P. Israelsen, and J. Muhs, "A review on inductive charging for electric vehicles," in *Proc. IEEE IEMDC*, 2011, pp. 143–147.
- [8] N. Tesla, "Apparatus for transmitting electrical energy," U.S. Patent 1 119 732, Dec. 1914.
- [9] A. Kurs *et al.*, "Wireless power transfer via strongly coupled magnetic resonances," *Science*, vol. 317, no. 5834, pp. 83–86, Jul. 2007.
- [10] H. Takanashi, Y. Sato, Y. Kaneko, S. Abe, and T. Yasuda, "A large air gap 3 kW wireless power transfer system for electric vehicles," in *Proc. IEEE Energy Convers. Congr. Expo.*, 2012, pp. 269–274.
- [11] C. Chih-Jung, C. Tah-Hsiung, L. Chih-Lung, and J. Zeui-Chown, "A study of loosely coupled coils for wireless power transfer," *IEEE Trans. Circuits Syst. II, Exp. Briefs*, vol. 57, no. 7, pp. 536–540, Jul. 2010.
- [12] A. P. Sample, D. A. Meyer, and J. R. Smith, "Analysis, experimental results, range adaptation of magnetically coupled resonators for wireless power transfer," *IEEE Trans. Ind. Electron.*, vol. 58, no. 2, pp. 544–554, Feb. 2011.
- [13] C. Sanghoon *et al.*, "Circuit-model-based analysis of a wireless energy-transfer system via coupled magnetic resonances," *IEEE Trans. Ind. Electron.*, vol. 58, no. 7, pp. 2906–2914, Jul. 2011.
- [14] W. Chwei-Sen, G. A. Covic, and O. H. Stielau, "Power transfer capability and bifurcation phenomena of loosely coupled inductive power transfer systems," *IEEE Trans. Ind. Electron.*, vol. 51, pp. 148–157, Feb. 2004.
- [15] Z. Yiming, Z. Zhengming, and C. Kainan, "Frequency decrease analysis of resonant wireless power transfer," *IEEE Trans. Power Electron.*, vol. 29, no. 3, pp. 1058–1063, Mar. 2014.
- [16] S. Li, W. Li, J. Deng, T. D. Nguyen, and C. C. Mi, "A double-sided LCC compensation network and its tuning method for wireless power transfer," *IEEE Trans. Veh. Technol.*, to be published.
- [17] M. Budhia, G. Covic, and J. Boys, "A new IPT magnetic coupler for electric vehicle charging systems," in *Proc. IEEE Ind. Electron. Soc. Conf.*, 2010, pp. 2487–2492.
- [18] M. Budhia, G. A. Covic, and J. T. Boys, "Design and optimization of circular magnetic structures for lumped inductive power transfer systems," *IEEE Trans. Power Electron.*, vol. 26, no. 11, pp. 3096–3108, Nov. 2011.
- [19] M. Budhia, J. T. Boys, G. A. Covic, and H. Chang-Yu, "Development of a single-sided flux magnetic coupler for electric vehicle IPT charging systems," *IEEE Trans. Ind. Electron.*, vol. 60, no. 1, pp. 318–328, Jan. 2013.

- [20] N. Trong-Duy, S. Li, W. Li, and C. C. Mi, "Feasibility study on bipolar pads for efficient wireless power chargers," in *Proc. IEEE Appl. Power Electron. Conf. Expo.*, 2014, pp. 1676–1682.
- [21] Z. Wei, W. Siu-Chung, C. K. Tse, and C. Qianhong, "Design for efficiency optimization and voltage controllability of series-series compensated inductive power transfer systems," *IEEE Trans. Power Electron.*, vol. 29, no. 1, pp. 191–200, Jan. 2014.
- [22] S. Hasanzadeh and S. Vaez-Zadeh, "Efficiency analysis of contactless electrical power transmission systems," *Energy Convers. Manag.*, vol. 65, pp. 487–496, Jan. 2013.
- [23] H. H. Wu, A. Gilchrist, K. D. Sealy, and D. Bronson, "A high efficiency 5 kW inductive charger for EVs using dual side control," *IEEE Trans. Ind. Informat.*, vol. 8, no. 3, pp. 585–595, Aug. 2012.
- [24] U. K. Madawala, M. Neath, and D. J. Thrimawithana, "A power-frequency controller for bidirectional inductive power transfer systems," *IEEE Trans. Ind. Electron.*, vol. 60, no. 1, pp. 310–317, Jan. 2013.
- [25] J. Hai, P. Brazis, M. Tabaddor, and J. Bablo, "Safety considerations of wireless charger for electric vehicles-A review paper," in *Proc. IEEE Symp. ISPCE*, 2012, pp. 1–6.
- [26] J. Yungtaek and M. M. Jovanovic, "A contactless electrical energy transmission system for portable-telephone battery chargers," *IEEE Trans. Ind. Electron.*, vol. 50, pp. 520–527, 2003.
- [27] A. Khaligh and S. Dusmez, "Comprehensive topological analysis of conductive and inductive charging solutions for plug-in electric vehicles," *IEEE Trans. Veh. Technol.*, vol. 61, no. 8, pp. 3475–3489, Oct. 2012.
- [28] J. Sallan, J. L. Villa, A. Llombart, and J. F. Sanz, "Optimal design of ICPT systems applied to electric vehicle battery charge," *IEEE Trans. Ind. Electron.*, vol. 56, no. 6, pp. 2140–2149, Jun. 2009.
- [29] J. L. Villa, J. Sallan, J. F. Sanz Osorio, and A. Llombart, "High-misalignment tolerant compensation topology for ICPT systems," *IEEE Trans. Ind. Electron.*, vol. 59, no. 2, pp. 945–951, Feb. 2012.
- [30] T. Imura, H. Okabe, and Y. Hori, "Basic experimental study on helical antennas of wireless power transfer for electric vehicles by using magnetic resonant couplings," in *Proc. IEEE Veh. Power Propul. Conf.*, 2009, pp. 936–940.
- [31] W. Chwei-Sen, G. A. Covic, and O. H. Stielau, "Investigating an LCL load resonant inverter for inductive power transfer applications," *IEEE Trans. Power Electron.*, vol. 19, no. 4, pp. 995–1002, Jul. 2004.
- [32] U. K. Madawala and D. J. Thrimawithana, "A bidirectional inductive power interface for electric vehicles in V2G systems," *IEEE Trans. Ind. Electron.*, vol. 58, no. 10, pp. 4789–4796, Oct. 2011.
- [33] N. A. Keeling, G. A. Covic, and J. T. Boys, "A unity-power-factor IPT pickup for high-power applications," *IEEE Trans. Ind. Electron.*, vol. 57, no. 2, pp. 744–751, Feb. 2010.
- [34] D. J. Thrimawithana and U. K. Madawala, "A generalized steady-state model for bidirectional IPT systems," *IEEE Trans. Power Electron.*, vol. 28, no. 10, pp. 4681–4689, Oct. 2013.
- [35] H. Pollock, "Simple constant frequency constant current load-resonant power supply under variable load conditions," *Electron. Lett.*, vol. 33, no. 18, pp. 1505–1506, 1997.
- [36] M. Borage, S. Tiwari, and S. Kotaiah, "Analysis and design of an LCL-T resonant converter as a constant-current power supply," *IEEE Trans. Ind. Electron.*, vol. 52, no. 6, pp. 1547–1554, Dec. 2005.
- [37] R. W. Erickson and D. Maksimovic, *Fundamentals of Power Electronics*, 2nd ed. New York: Kluwer, 2001.
- [38] L. Bing, L. Wenduo, L. Yan, F. C. Lee, and J. D. Van Wyk, "Optimal design methodology for LLC resonant converter," in *Proc. IEEE Appl. Power Electron. Conf. Expo.*, 2006, p. 6.



Han Zhao received the B.S. and M.S. degrees in mechanical engineering from Hefei University of Technology, Hefei, China, in 1982 and 1984, respectively, and the Ph.D. degree in mechanical engineering from Aalborg University, Aalborg, Denmark, in 1990.

He is the Vice President of Hefei University of Technology. His research interests include mechanical transmission, digital design and manufacturing technology, information systems, dynamics and control, automotive systems, and

electric vehicles.



Siqi Li (M'13) received the B.S. and Ph.D. degrees in electrical engineering from Tsinghua University, Beijing, China, in 2004 and 2010, respectively.

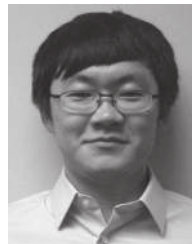
He was a Postdoctoral Fellow with the University of Michigan, Dearborn, MI, USA, from 2011 to 2013. In 2013, he joined the Faculty of Electric Power Engineering, Kunming University of Science and Technology, Kunming, China, where he is currently a Lecturer with the Department of Electrical Engineering. Also, he is

the Director of the Advanced Power Electronics and New Energy Laboratory. His research interest focuses on battery management systems and high-performance wired and wireless battery chargers for electric vehicles.



Junjun Deng (S'13–M'14) received the B.S. and M.S. degrees in electrical engineering from Northwestern Polytechnical University, Xi'an, China, in 2008 and 2011, respectively, where he is currently working toward the Ph.D. degree in electrical engineering.

From 2011 to 2013, he was a joint Ph.D. student funded by the China Scholarship Council with the University of Michigan, Dearborn, MI, USA. He was a Research Assistant with the Department of Electrical and Computer Engineer, University of Michigan. His research interests include wireless power transfer, resonant power conversion, and high-performance battery chargers for electric vehicles.



Tianze Kan received the B.Eng. degree in electrical engineering and automation from Huazhong University of Science and Technology, Wuhan, China, in 2011 and the M.S. degree in electrical engineering (electric power) from the University of Southern California, Los Angeles, CA, USA, in 2013. He is currently working toward the Ph.D. degree in automotive systems engineering in the Department of Electrical and Computer Engineering, University of Michigan, Dearborn, MI, USA.

His current research interests include power electronics and wireless power transfer.



Chunting Chris Mi (S'00–A'01–M'01–SM'03–F'12) received the B.S.E.E. and M.S.E.E. degrees in electrical engineering from Northwestern Polytechnical University, Xi'an, China, and the Ph.D. degree in electrical engineering from the University of Toronto, Toronto, ON, Canada.

He is a Professor of electrical and computer engineering and the Director of the Department of Energy-funded Graduate Automotive Technology Education Center for Electric Drive

Transportation, University of Michigan, Dearborn, MI, USA. Prior to joining the University of Michigan in 2001, he was with General Electric Company, Peterborough, ON, Canada. His research interests include electric drives, power electronics, electric machines, renewable-energy systems, and electrical and hybrid vehicles. He has conducted extensive research and has published more than 100 journal papers.

Dr. Mi is an Area Editor of the IEEE TRANSACTIONS ON VEHICULAR TECHNOLOGY and an Associate Editor of the IEEE TRANSACTIONS ON POWER ELECTRONICS and IEEE TRANSACTIONS ON INDUSTRY APPLICATIONS.



Weihan Li (S'13) received the B.S. degree in automotive engineering from Hefei University of Technology, Hefei, China, in 2010, where he is currently working toward the Ph.D. degree in automotive engineering.

From September 2012 to August 2014, he was a joint Ph.D. student funded by the China Scholarship Council with the Graduate Automotive Technology Education Center for Electric Drive Transportation, Department of Electrical and Computer Engineering, University of Michigan,

Dearborn, MI, USA, where he was involved in the modeling and design of a wireless charger for electric vehicles (EVs)/plug-in hybrid electric vehicles (PHEVs). His research interests include wireless power transfer, EV/PHEV systems, renewable energy, and power electronics.